AGU ADVANCING EARTH AND SPACE SCIENCES

JGR Oceans

RESEARCH ARTICLE
10.1029/2023JC020385

Key Points:

- The spatial distribution of internal tides in the northern South China Sea is revealed by a fleet of underwater gliders
- Propagation distances exceeding 1,000 km and wavelengths of ~300 km for mode-1 diurnal tides were directly observed
- The dissipation of the mode-1 diurnal internal tides induces a dissipation rate of ~10^{-8} W/kg in the far-field

Correspondence to:
Z. Chen,
chenzhaohui@ouc.edu.cn

Citation:
Gao, Z., Chen, Z., Huang, X., Yang, H., Wang, Y., Ma, W., & Luo, C. (2024). Estimating the energy flux of internal tides in the northern South China Sea using underwater gliders. *Journal of Geophysical Research: Oceans*, *129*, e2023JC020385. https://doi.org/10.1029/2023JC020385

Received 18 AUG 2023
Accepted 22 JAN 2024

Author Contributions:
Conceptualization: Zhiyuan Gao, Zhaohui Chen
Data curation: Zhiyuan Gao, Zhaohui Chen, Yanhui Wang, Wei Ma, Chenyi Luo
Formal analysis: Zhiyuan Gao, Zhaohui Chen, Xiaodong Huang
Funding acquisition: Zhaohui Chen, Yanhui Wang, Wei Ma
Methodology: Zhiyuan Gao, Zhaohui Chen, Haiyuan Yang, Chenyi Luo
Project administration: Zhaohui Chen
Software: Zhiyuan Gao
Supervision: Zhaohui Chen
Validation: Zhiyuan Gao, Zhaohui Chen
Visualization: Zhiyuan Gao
Writing – original draft: Zhiyuan Gao
Writing – review & editing: Zhiyuan Gao, Zhaohui Chen, Xiaodong Huang, Haiyuan Yang

Estimating the Energy Flux of Internal Tides in the Northern South China Sea Using Underwater Gliders

Zhiyuan Gao[1], Zhaohui Chen[1,2], Xiaodong Huang[1,2], Haiyuan Yang[1,2], Yanhui Wang[2,3], Wei Ma[2,3], and Chenyi Luo[3]

[1]Frontier Science Center for Deep Ocean Multispheres and Earth System (FDOMES) and Physical Oceanography Laboratory, Ocean University of China, Qingdao, China, [2]Laoshan Laboratory, Qingdao, China, [3]Key Laboratory of Mechanism Theory and Equipment Design Ministry of Education, School of Mechanical Engineering, Tianjin University, Tianjin, China

Abstract The characteristics of the energy flux of internal tides in the northern South China Sea (SCS) were explored by analyzing a fleet of underwater gliders. It was found that the low-mode diurnal internal tides with ~300 km wavelength in the middle basin are generated predominantly in the Luzon Strait (LS) and propagate over 1,000 km to the western SCS. However, the semidiurnal internal tides are generated in multiple regions, including the LS in the east part, the continental shelf, and the islands in the west. The energy flux of the mode-1 diurnal internal tides attenuated rapidly within 450 km of the LS and was less pronounced after that. The estimated dissipation rate based on the mode-1 energy flux is about 10^{-8} W/kg, underling the significant role of mode-1 diurnal internal tides in bolstering far-field mixing. This study provides a unique view of the spatial pattern, energy flux, and energy sink of the internal tides in the northern SCS, which could supplement the altimetry-based results and improve the parameterization in ocean models.

Plain Language Summary The South China Sea (SCS), is situated near the Luzon Strait (LS)—the global ocean's most active region for internal tide generation. It is abundant with internal tides. However, there is a notable lack of understanding regarding the spatial distribution of the energy flux of these internal tides in the SCS, as determined by in-situ observations. Our study, based on data collected from a fleet of underwater gliders, revealed that internal tides of diurnal frequency can propagate to the western continental shelf of the SCS, exhibiting a significant mode-1 vertical structure. In contrast, semidiurnal internal tides originated from multiple sources. We observed that energy decay occurs rapidly within 500 km of the source, while it exhibited relatively slow decay in the central region of the basin. By correlating the energy attenuation with dissipation, we found that the depth-averaged dissipation rate aligns with the directly observed value. This suggested that the mode-1 diurnal internal tides may effectively enhance the far-field mixing in the northern SCS.

1. Introduction

Internal tides, internal waves with tidal frequencies, provide half of the energy (~1 TW) for maintaining the deep ocean stratification and thus play an important role in the Meridional Overturning Circulation (Munk & Wunsch, 1998). Low-mode internal tides can propagate thousands of kilometers while most high-mode internal tides are typically dissipated locally (Alford, 2003; Klymak et al., 2006; Rainville & Pinkel, 2006; Z. Zhao et al., 2010). It has been noted by Vic et al. (2019) that small-scale (high mode) internal tides contribute to global deep ocean mixing efficiently, while lower mode internal tides exert more significant impacts on distant ocean mixing far from the source regions.

The South China Sea (SCS), the largest marginal sea in the Western Pacific, is well-known for its energetic internal tides (Alford et al., 2015). Low-mode internal tides are generated in the Luzon Strait (LS) and propagate to the interior of the SCS (Klymak et al., 2011; Li & Xie, 2023; Wang, Cao, et al., 2021). Z. Zhao (2014) successfully mapped the energy flux pattern of internal tides in the SCS based on satellite altimeter observations. He emphasized that the internal tides generated at the LS could travel over 1,600 km before reaching the coast of Vietnam. Modeling results reveal the characteristic of long-distance propagation of diurnal internal tides in the SCS (Xu et al., 2016). R. Zhao et al. (2018) indicated the presence of distinct sources generating diurnal and semidiurnal internal tides, based on indirect observations in the western SCS. However, there is still a lack of understanding regarding the nature of long-distance propagation, energy attenuation, and the role of internal tides in mixing within the SCS due to insufficient in-situ observations.

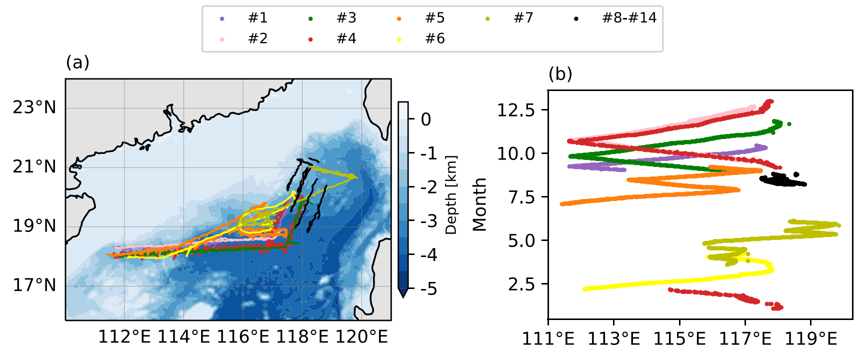

Figure 1. (a) Trajectories of underwater gliders. (b) Longitudinal location of each underwater glider as the function of months.

In recent decades, underwater gliders have been widely used in in-situ observations regarding multiple oceanic processes and are proven to be promising instruments for detecting internal tides (Johnston et al., 2013; Rudnick, 2016). In regions full of active internal tides, for example, Rainville et al. (2013) estimated the spatial structure of energy flux of internal tides around the LS. In the Tasman Sea, Boettger et al. (2015) characterized the spatial structure of semidiurnal internal tides near the coast of Tasman, and Johnston et al. (2015) investigated the standing wave pattern of internal tides. Besides, underwater gliders also enable us to investigate the high-frequency internal waves and mixing (Johnston & Rudnick, 2015; Rudnick et al., 2013) owing to their high-frequency sampling capability.

To reveal the spatial distribution of energy flux of internal tides in the northern SCS, 14 Petrel underwater gliders, designed by Tianjin University (F. Liu et al., 2017; Wang, Yang, et al., 2021), were successively deployed in the northern part of SCS from 2017 to 2021 as sea trial campaigns. Based on these data, we characterized the spatial distribution of mode-1 internal tides and estimated its energy flux as well as the associated contributions to mixing the ocean. The rest of this paper is organized as follows: Section 2 briefly introduces the data retrieved from the underwater gliders. Section 3 describes the observed spatial pattern of vertical displacement induced by internal tides. In Section 4, the spatial distribution of mode-1 energy flux of internal tides is revealed and their roles in mixing are discussed. Section 5 estimates the errors from imperfect vertical resolutions and the plane wave fit method. Section 6 gives a discussion and conclusion.

2. Data

Between 2017 and 2021, a fleet of 14 Petrel underwater gliders, equipped with Glider Payload CTDs (GPCTDs), were sequentially deployed in the northern part of the SCS. Seven of these gliders, denoted as #1–#7, conducted profiling missions along the east-west direction between longitudes 111°E and 118°E. The remaining seven gliders, identified as #8–#14, were stationed at approximately 118°E longitude, profiling the region between 18°N and 22°N (Figure 1).

The typical sampling intervals between adjacent dives for gliders #1–#7 and #8–#14 are approximately 5 and 2 hr, respectively. These intervals can accurately capture the semidiurnal and diurnal internal tides, given that the frequency of semidiurnal internal tides is roughly 1/12 cycles per hour (cph). Each profile's horizontal interval spans 1–2 km, a sufficient range to detect the lower mode internal tides, which commonly have wavelengths between 100 and 300 km in this region.

These underwater gliders have successfully obtained over 8,000 profiles of temperature, salinity, and pressure, with data collected during both the upward and downward journeys used in this study. The maximum sampling depth varied between 297 and 1,018 m during these missions, with the majority of the effective profiles exceeding a depth of 800 m for gliders #1–#7 and 600 m for gliders #8–#14. Moreover, the GPCTD's vertical sampling frequency is 1 Hz, hence its vertical resolution is approximately 1 m. Ultimately, data from these underwater gliders were averaged in a 10-m vertical bin from the surface to their respective maximum sampling depths. Note that the CTD data are quality-controlled by detecting the anomaly conductivity values and thermal lag correction (Liu et al., 2020).

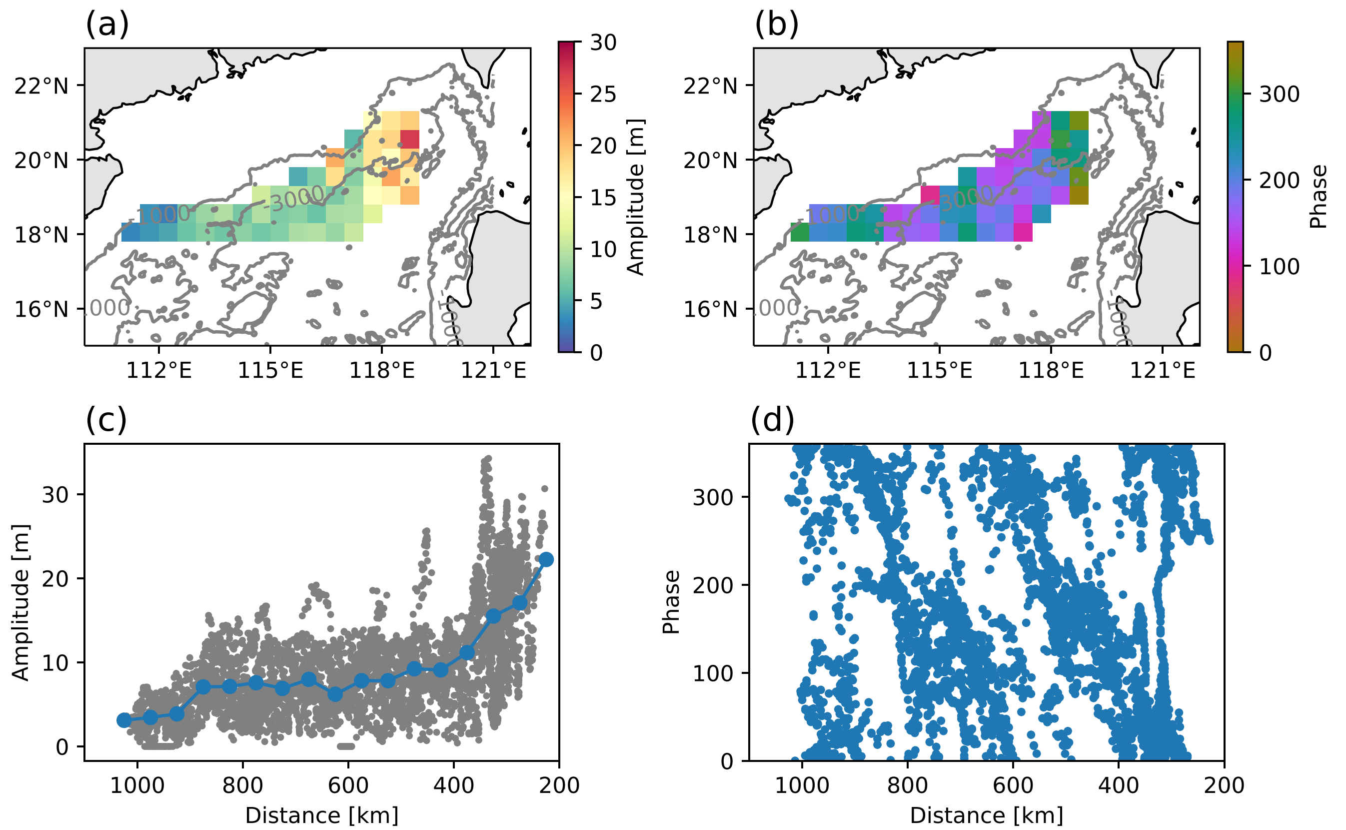

Figure 2. Spatial distribution of (a) amplitude and (b) phase of isopycnal vertical displacements induced by diurnal internal tides at 500 m. (c) and (d) are scatterplots showing the amplitude and phase of the diurnal internal tides, respectively, as functions of distance from the Luzon Strait. The blue dots represent the average values in (c).

3. Spatial Distribution of Amplitude and Phase

To obtain the vertical displacements induced by internal tides and the resultant energy flux, the isopycnal vertical displacements $\eta(z,t) = g\Delta\sigma_\theta/\sigma_\theta\langle N^2\rangle$ were derived using observed temperature and salinity data. Here, g is the acceleration of gravity, σ_θ represents the potential density, N^2 stands for the square of the buoyancy frequency, and <> denotes the 3-day average. Subsequently, harmonic analysis is performed to discretize the vertical displacements at semidiurnal and diurnal frequencies:

$$\eta(z,t) = \sum\nolimits_{j=\mathrm{SD},D} \left(H_j(z) \cos\left(\sigma_j t - g_j(z)\right)\right) \tag{1}$$

where H_j(z) and g_j(z) are the amplitude and phase of cosine wave package at frequency σ_j. In this context, M_2 (1/12.4206 hr^{-1}) and K_1 (1/23.9345 hr^{-1}) are selected as the primary representatives of the semidiurnal and diurnal constituents, respectively. Due to the differing sampling intervals between adjacent dives for groups #1–#7 and #8–#14, a moving harmonic analysis of 27 points and 53 points was employed for these two data sets respectively, ensuring an approximately 3-day window. The amplitude and phase of isopycnal vertical displacements for semidiurnal and diurnal internal tides were subsequently binned into a 1/2° by 1/2° box, which roughly corresponds to 1/6 of the wavelength of mode-1 diurnal internal tides (as shown in Figures 2a and 2b).

Figure 2a illustrates that the spatial distribution of amplitude remains largely consistent around 119°E, suggesting widespread generation of diurnal internal tides with significant amplitude at the LS from north to south. At a depth of 500 m, the isopycnal vertical displacements typically diminish as one moves away from the LS, with a displacement of approximately 20 m at 119°E and a mere 5 m at 112°E. Notably, the most pronounced reduction in mean amplitude is observed within 500 km of the LS and 800 km west of the LS (Figure 2c). In contrast, the amplitude remains stable between these two regions. The efficient decay of isopycnal vertical displacement is manifested by shrinking of tidal energy, which may be attributed to the tidal interaction with local topography and

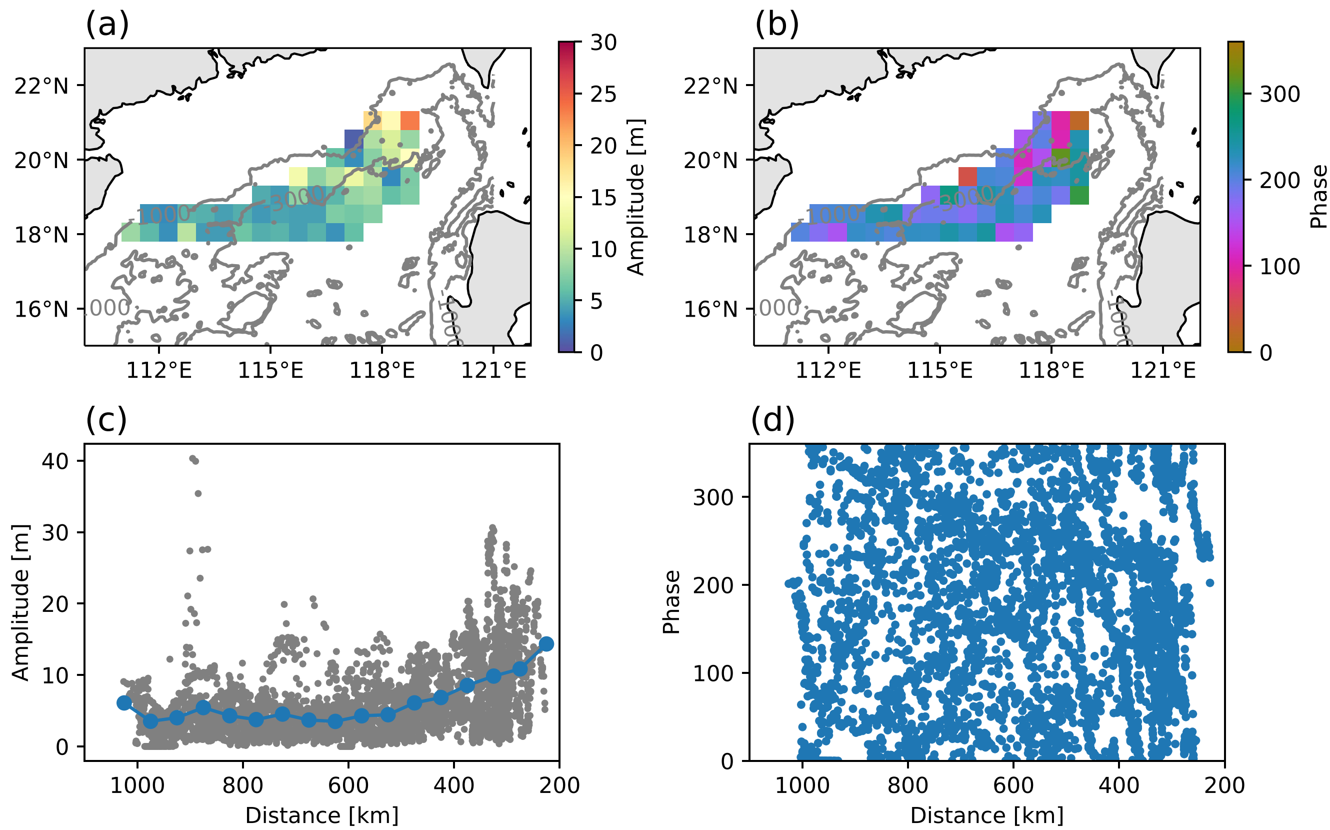

Figure 3. As in Figure 2, but for semidiurnal internal tides.

the advection of the tidal energy since the parametric subharmonic instability (PSI) may not play a role at these latitudes (the diurnal critical latitude of PSI locates roughly at 14.52°N).

The wavelength of approximately 300 km in the middle basin can be easily determined by the phase shift, aligning with the characteristics of mode-1 diurnal internal tides in this region (Figure 2b). The spatial distribution of phase bears a striking resemblance to the mode-1 pattern map derived by Z. Zhao (2014) using satellite altimeter data, and the estimated phase speed aligns well with the theoretical phase speed (Figure 2d) when examining the relationship between the phase and distance to the LS (note that the distance is calculated from a starting point at 20.5°N, 121°E). These findings suggest that the diurnal internal tides generated at the LS are notably strong and can traverse over 1,000 km before reaching the western continental shelf.

The amplitude of isopycnal vertical displacements for semidiurnal tides is quite weak compared to the diurnal internal tides (Figure 3). The relatively large amplitudes focus on the eastern of 117°E and are nearly uniform in the western area. The prominent spring-neap cycle also occurs at the easternmost part with the largest amplitude reaching 30 m. In general, the mean isopycnal vertical displacement amplitude of semidiurnal internal tides is about half of diurnal internal tides. Both the spring-neap cycle and the decay trend from LS are weaker than the diurnal internal tides. The phase is disordered and cannot be clearly distinguished due to multi-generations and incoherent partition of the energy. Specifically, the source of semidiurnal internal tides may be generated from multi-regions and this distinguished these phase distribution results from the multi-wave interference. Besides, the comparable scale of the mode-1 semidiurnal internal tides with the mesoscale motions makes it more easily influenced by the mesoscale eddies and background currents, which enhance the incoherence of the semidiurnal internal tides (Huang et al., 2018).

4. Mode-1 Energy Flux

Due to the complex vertical structure and lower phase speed, the highest mode (high wave number) internal tides quickly dissipate after their generations. Considering the lower mode internal tides can propagate thousands of

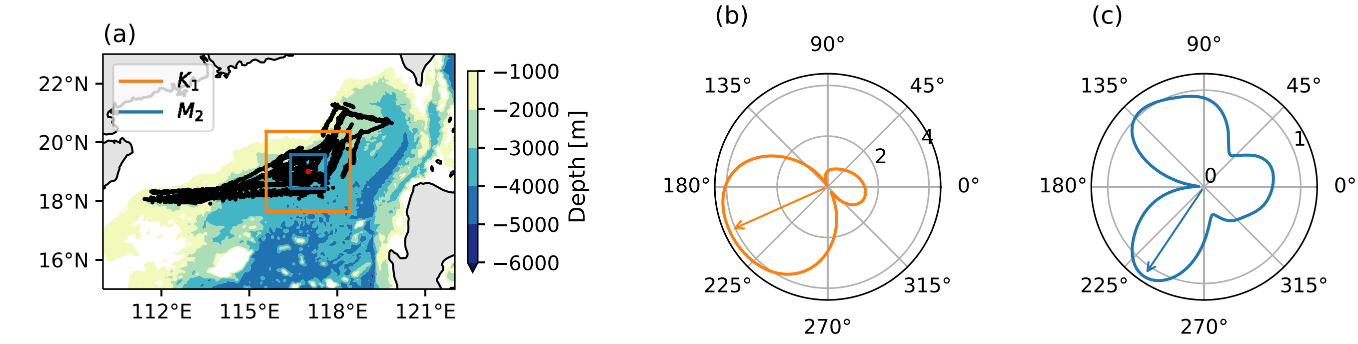

Figure 4. An example of plane wave fit at 500 m at 118°E, 20°N. (a) The region size of plane wave fit for K_1 and M_2 internal tides is 300 km × 300 km (orange), and 125 km × 125 km (blue), respectively. The red dot within the fitting region denotes the center point of the plane wave fit. (b) Amplitude as a function of propagation direction for K_1. (c) As in panel (b), but for M_2. Arrows in panels (b) and (c) denote the propagation of the largest amplitude.

kilometers from their generation sites (Z. Zhao et al., 2010), it is beneficial to assess how much energy the lower mode internal tides carry (i.e., energy flux) and dissipate (i.e., resultant diapycnal mixing) during their long-distance propagation. To obtain the mode-1 energy flux, the mode-1 isopycnal vertical displacements are calculated, in which the vertical modes can be determined by solving the eigenvalue equation (Gill, 1982)

$$\Phi''(z) + \frac{N^2(z)}{c^2}\Phi(z) = 0, \tag{2}$$

constrained by rigid lid boundary condition $\Phi(-\mathrm{H}) = \Phi(0) = 0$, where $\Phi(z)$ is the vertical structure function, c is the eigenvalue and N^2 is the square of buoyancy frequency. Since the underwater gliders only dove to the depth of 1,000 m, the full-depth N^2 using the World Ocean Atlas 2018 (WOA18) data is calculated. The vertical displacements can be written as:

$$\eta'(x,y,z,t) = \sum_{n=1}^{\infty} A_n(x,y,t)\Phi_n(z), \tag{3}$$

where A_n denotes the nth mode amplitude that is obtained by least squares fitting and Φ_n denotes the vertical structure of the nth mode. However, due to the limited maximum sampling depth by underwater gliders, the

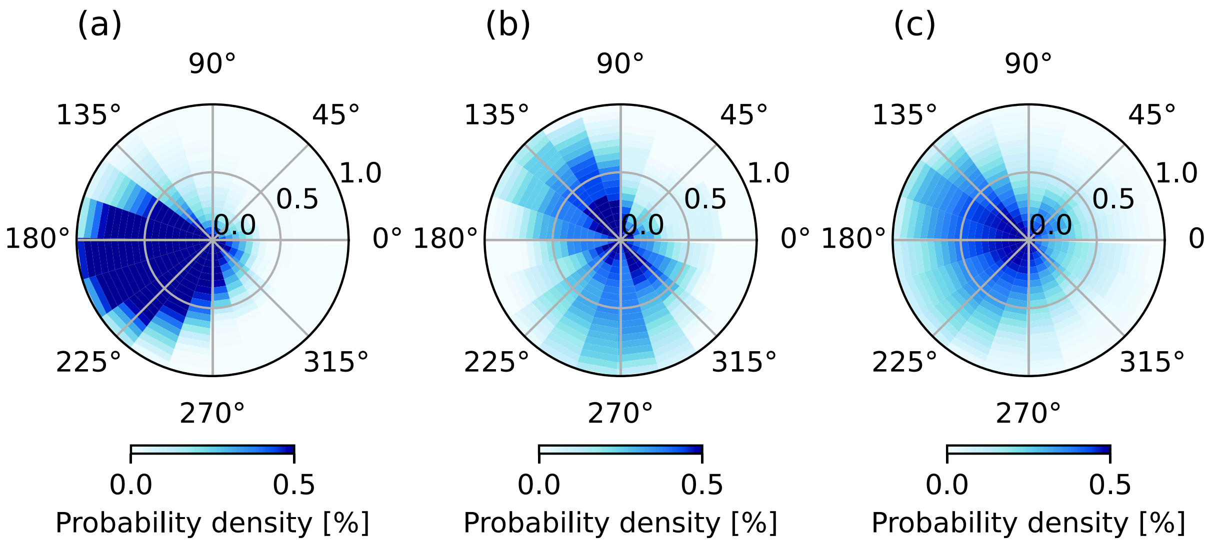

Figure 5. The composite results of amplitude as the function of propagation direction at 500 m. The amplitude is scaled to 0–1 by the maximum value. (a), (b) and (c) are results for K_1, M_2 (111.5°E−114°E) and M_2 (114°E−119°E), respectively.

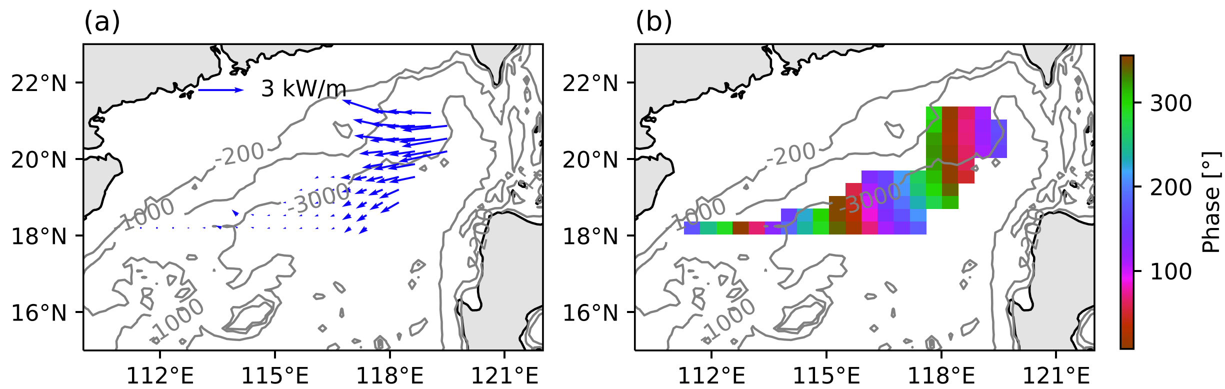

Figure 6. Mode-1 energy flux (left) and phase (right) of K_1 internal tides.

higher mode structure cannot be resolved especially in the deep basin. Here, only the mode-1 vertical displacements (η'_1) are discussed. The error of the mode decomposition will be discussed in Section 5. The magnitude of energy flux of internal tides can be computed from $F = C_g E$, where E is the sum of Available Potential Energy (APE) and Horizontal Kinetic Energy (HKE). C_g denotes the group velocity and is determined by $C_g = c\left(\omega^2 - f^2\right)^{1/2}/\omega$, where ω is the tidal frequency and c denotes the eigenvalue derived from Equation 2. If assuming the internal tides are progressive waves, the energy flux can be easily calculated from the relation between APE and HKE. Therefore, the η'_1 in different propagation paths should be distinguished. Thus, we use the plane wave fit method, an effective technique to separate different beams of internal tides from different sources, which has been used in multisource satellite altimetry data (Z. Zhao, 2014; Z. Zhao et al., 2016), to tackle this issue. For each propagation direction θ, the η'_1 is the function of the amplitude a and the phase ϕ, and it can be described as the plane wave format as follows

$$\eta'_1(a,\phi,\theta) = a\cos(k_1 x\cos\theta + k_1 y\sin\theta - \omega t - \phi), \tag{4}$$

where k_1 and ω are the mode-1 wave number and frequency of the internal tides. The horizontal wave number of mode-1 internal tides is obtained by solving the eigenvalue equation. Thus, the amplitude and phase at each propagation direction are calculated with the plane wave fitting and enumeration method. To ensure sufficient resolution of the mode-1 wave and assure small spatial smooth of the result, choosing one wavelength of the

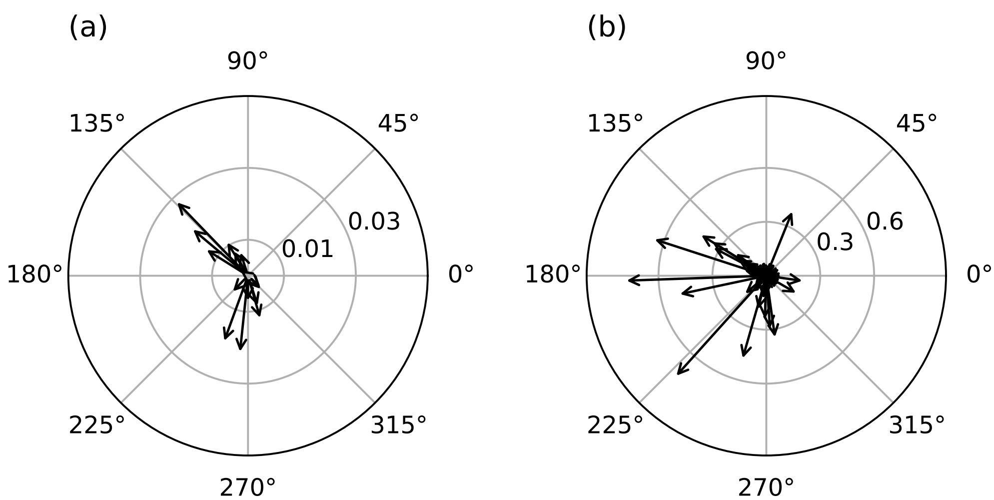

Figure 7. Polar diagram of the mode-1 M_2 energy flux as function of propagation direction at 111.5°E−114°E (a) and at 114°E−119°E (b).

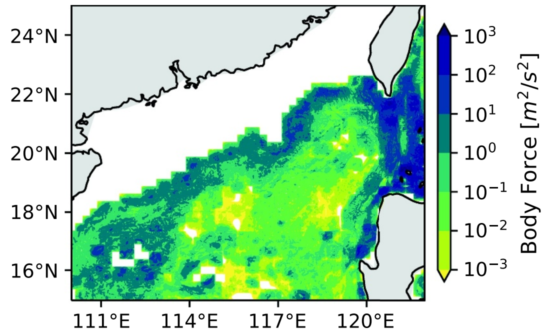

Figure 8. Barotropic tidal body force at M_2 frequency.

mode-1 internal tides as the size of the fit window is reasonable. The sensitivity of this fit window will be discussed in Section 5. The size of the fit window for one wavelength can't distinguish O_1 internal tides effectively, which may be due to its relatively weak energy and the large bent of the energy beam.

One example of the plane wave fit method at 118°E, 20°N is shown in Figure 4. At this region, the mode-1 wavelength of K_1 and M_2 is about 308 and 125 km, respectively. For K_1 internal tides, the maximum amplitudes occur in the western direction which denotes its main propagation. For the M_2 internal tide, the relatively strong amplitudes occur in two different directions. The composite propagation directions of K_1 internal tide are consistently westward. This indicates that the LS is the most powerful source of mode-1 energy of diurnal internal tides (Figure 5a). The M_2 internal tides in the northern SCS within the different regions may be produced from different sources (Figures 5b and 5c). At 111.5°E−114°E, the main propagation direction is northward and southward, which indicates the tidal energy generated from the northern continental shelf and the southern island. At 114°E−119°E, the strongest amplitude occurs in the northwestern direction with weak southwestern beams, which indicates a strong energy source from LS. Due to the main propagation direction of diurnal internal tides being westward only, the first-round plane wave fit

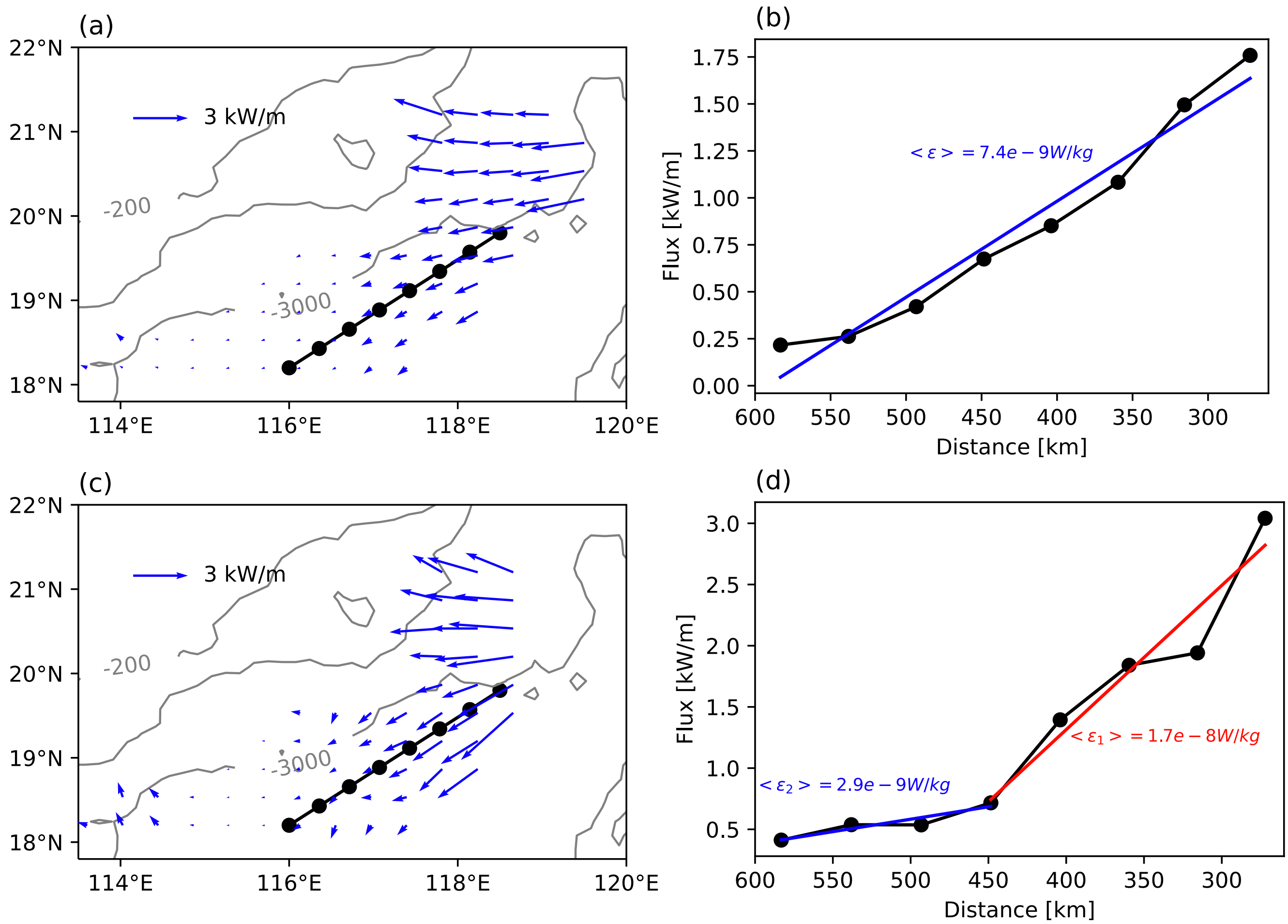

Figure 9. Energy flux of K_1 internal tide (a), (c) and its linear fit along the beam (b), (d). The top panel is the result under the one-wavelength plane wave fit while under half-wavelength for the low panel. The contour lines are the topography at 200, 1,000, and 3,000 m. The black lines in panels (b) and (d) denote the energy flux along the beam (a, c, black lines) as the function of distance from Luzon Strait (20.5°N, 121°E). The red and blue lines denote the linear fit results. $<\varepsilon>$, $<\varepsilon_1>$, and $<\varepsilon_2>$ are the estimated depth-averaged diapycnal dissipation rates of different regions from the linear fit of the energy flux along the beam.

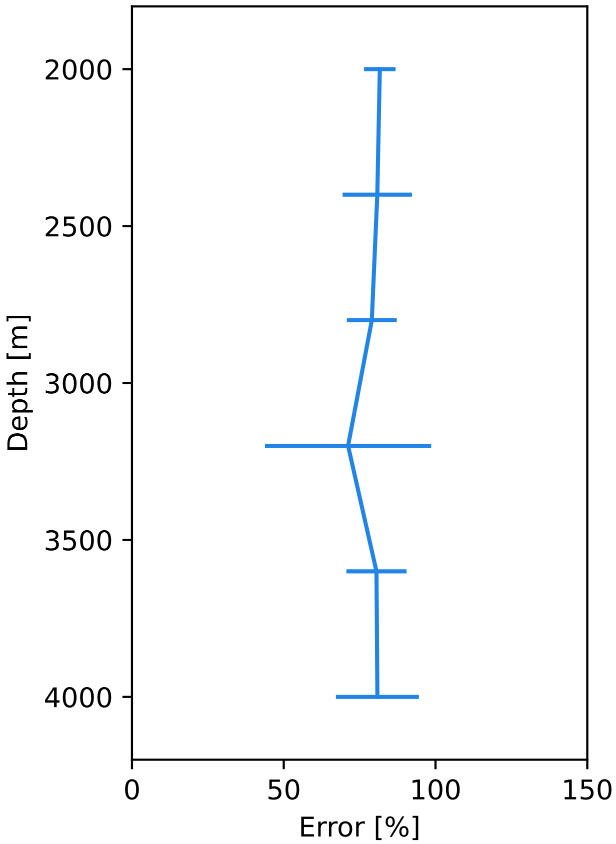

Figure 10. The median and standard error of mode-1 Available Potential Energy in one period versus the water depth.

method is used and the direction in which the maximum amplitude occurs is selected (Figure 4). For the M_2 internal tide, there are multiple propagation directions with prominent amplitudes. Therefore, fitting is processed again and two maximum amplitudes and phases are selected.

The magnitude of energy flux at each location can be derived from:

$$|\mathbf{F}| = \frac{\rho_0 c}{2} \frac{\omega}{(\omega^2 - f^2)^{1/2}} \int_0^H N^2(z) Am^2(z)\, dz, \tag{5}$$

where H is the water depth, ρ_0 is the mean seawater density, c is the eigenvalue derived from (2) and $Am\ (z)$ is the amplitude calculated from the plane wave fit method. The propagation direction of the energy flux also has been derived from the plane wave fit method.

After mode decomposition and plane wave fit are applied, the spatial distribution of mode-1 K_1 character is much clearer than through harmonic analysis (Figure 6). Generated from the LS, the K_1 internal tide propagates westward to the northern continental shelf and the deep basin of the SCS. The magnitude of the mode-1 energy flux is about 3 kW/m at 119°E. It disappears at the western continental shelf although there is a weak increase around 114°E. This increased energy may originate locally or remotely. Along the propagation path, the energy flux decays quickly as it propagates into the deep basin. The isophase lines show the prominent mode-1 K_1 character with northeastern-southwestern propagation direction in the middle basin. In the middle basin, the mode-1 K_1 is characterized by ~300 km wavelength while decreasing in the western shallow water region.

For M_2 internal tide, the magnitude is one order weaker than K_1 internal tide (Figure 7). The propagation direction of the energy flux is mainly from north to south between 111.5°E−114°E while it is from east to west between 114°E−119°E. To demonstrate the generating source, the tidal body force is calculated by $F = Q \cdot \nabla H \cdot N_b^2/\omega$, where Q is the barotropic tidal transport from TPXO9 (Egbert & Erofeeva, 2002), ∇H is the gradient of the topography from SRTM15 + v2.0 (Tozer et al., 2019), N_b^2 is the squared bottom bouncy frequency from WOA18, and ω is the tidal frequency. The spatial distribution of the barotropic tidal force is shown in Figure 8. The LS, the continental shelf and the islands in the SCS are both energy sources of M_2 internal tide. Strong internal tide energy is produced at the northern continental shelf and the southern island, which take up most of the fraction of the observed M_2 energy in the western basin. This is proven by the observed energy flux in the north-south directions. In the eastern basin of the SCS, it is the internal tide produced from LS occupies the main fraction of the observed mode-1 energy flux.

The energy flux of K_1 internal tide is attenuating as it propagates to the western continental shelf. The contribution of mode-1 internal tides to diapycnal mixing in the northern SCS based on the energy flux is quantified (Figure 4d). Assuming that the tidal energy is unchanged with time and the advection of energy is negligible, the energy density equation can be simply written as:

$$0 = \nabla \cdot \boldsymbol{F} + E - \varepsilon, \tag{6}$$

where $\boldsymbol{F}$, E, and ε are energy flux, energy conversion from barotropic to baroclinic tidal currents and local dissipation rate, respectively. In this sense, the upper limit of ε can be estimated by neglecting the locally generated baroclinic energy considering the net energy flux balance. The gradient of mean energy flux across the energy beam can be simplified as the function of water depth, so the depth-averaged dissipation rate $<\varepsilon>$ is then derived.

Two different plane wave fit processes with different windows are applied given that the plane wave fit may smooth the spatial distribution of the energy flux (Figure 9). For a window size of one wavelength, an

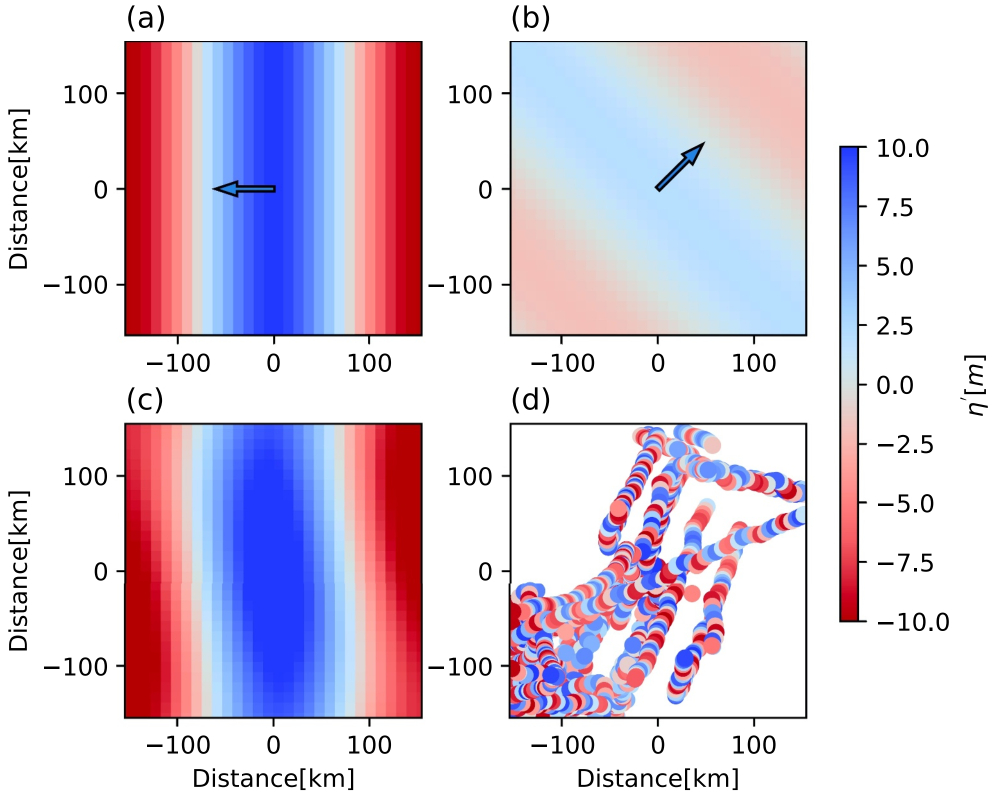

Figure 11. A plane wave fit example of two ideal K_1 waves with different propagation and vertical amplitude. (a) Westward propagation wave with vertical amplitude of 10 m and horizontal wavelength of 309 km. (b) Waves with amplitude of 5 m and 45° direction relative to the *x*-axis. (c) Sum wave of (a) and (b). (d) The glider's sampling for the superimposed wave in panel (c). The center point is 118°E, 20°N and the length of the box is one wavelength of mode-1 K_1 internal tide. The arrows in panels (a) and (b) denote the propagation direction.

estimated energy flux $<\varepsilon>$ is 7.4×10^{-9} W/kg. The energy decay rate is almost consistent along the selected beam in this case, which may be influenced by the smooth effect of the plane wave fit. To increase the resolution of the spatial distribution of the energy flux, data with the window size of half of the mode-1 wavelength is processed. In this case, the energy decays fast within 450 km and slow beyond that. The estimated $<\varepsilon>$ is 1.70×10^{-8} W/kg within 450 km of the LS and 2.9×10^{-9} W/kg after that. The order of the estimated $<\varepsilon>$ is approximately consistent with estimations by in-situ observations in this region (Y. Liu et al., 2017; Lu et al., 2021; Tian et al., 2009). This implies the dissipations of mode-1 internal tides elevated the far-field mixing in the SCS as they propagate westward.

5. Errors

5.1. Errors of the Vertical Mode Decomposition

The sampling depth of underwater gliders is about 1,000 m, while the vertical mode is the solution under the boundary condition of the full water depth. Different from the mooring, the glider observed data have more continuity vertically while it has a large bottom gap limited by its finite sampling depth. Nash et al. (2005) estimated the error with a series of bottom gaps, which revealed that more error occurs with fitting with more mode numbers at the fixed depth. To minimize the fitting error, only mode-1 internal tides are considered in this study. Following Nash et al. (2005), a series of synthetic internal tides are produced by superposing 30 vertical modes and red noise. The Monte Carlo method is applied on the synthetic signal which is each vertical mode in a random phase. The errors of mean mode-1 APE in one tidal period at each depth are almost consistent, with median values of 70%–80% (Figure 10).

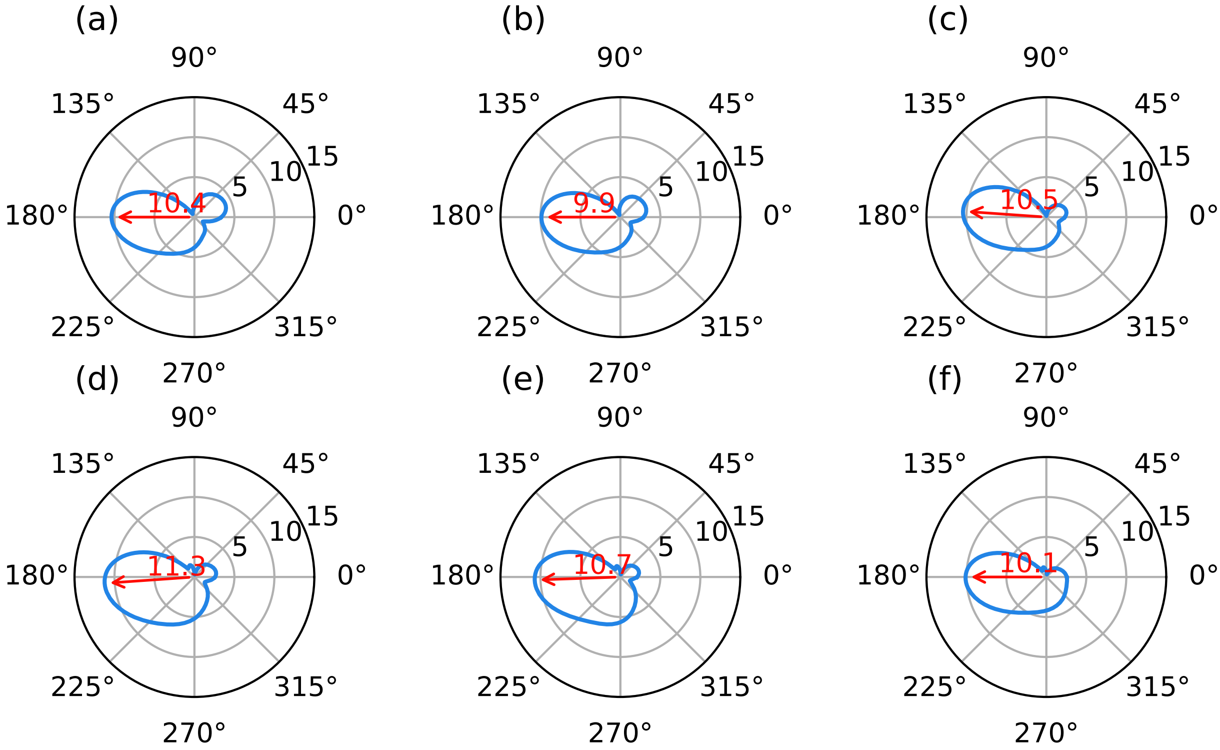

Figure 12. Polar diagrams of amplitudes as the function of propagation directions derived from the plane wave fit of vertical displacement within Figure 11d. Different subfigures denote the fitting wave with waves propagating on 180° and 45° (a), 90° (b), 135° (c), 225° (d), 270° (e), and 315° (f). The propagation directions and amplitude of the wave are shown by red arrows and numbers, respectively.

5.2. Errors of the Plane Wave Fit Method

Since the underwater glider is not equipped with a current meter instrument, the energy flux cannot be directly calculated from the velocity and pressure anomaly. In this study, the plane wave fit method is used to separate the internal tides in different propagation directions and then the energy flux is estimated from the relation of APE and KE. This method is widely used in separating the different propagation internal tides in the satellite altimeter data (e.g., Z. Zhao, 2014). To ensure the best fitting window size in separating the different propagation directions, a series of ideal plane wave fit experiments are considered.

Considering that most of the K_1 energy is produced from LS and a few may be from the continental shelf, two superimposed plane waves are considered (Figure 11). The first wave propagates to the westward with an amplitude of 10 m. The second wave has an amplitude of 2 m and a variable propagation direction. The order of the assumed amplitude is consistent with the observed results of ∼10 m. The data collected by the underwater glider are time-space aliased and the sampling points are unevenly distributed. The results of the plane wave fit may vary in different regions because of the different spatial distributions of the trajectories. Here the region centered at 118°E, 20°N is selected and noted that the following results are mostly consistent in other regions. In this region, the wavelength of mode-1 K_1 internal tide is about 309 km. The plane wave fit method is applied to the ideal vertical displacements sampled according to the real glider trajectories. Each amplitude as the function of propagation results is shown in Figure 12. For different ideal waves, the plane wave fit method with the fitting size of one wavelength could identify the propagation direction with the maximum amplitude while the errors are relatively large when the angle between the two waves is smaller than 45°. The minimum amplitude error is smaller than 0.1 m and the maximum error is 0.7 m. Decreasing the relative angle and amplitude between the two waves will increase the error and make the waves harder to distinguish.

Previous studies indicated that the semidiurnal internal tides may have multi-sources besides the LS (Z. Zhao, 2020). Here, to determine the plane wave fit region enough to detect M_2 internal tides with different propagation directions, the ideal exercise of two plane waves with different propagation directions and amplitudes is considered. A wave superimposed by a westward wave with an amplitude of 10 m and a changed direction wave

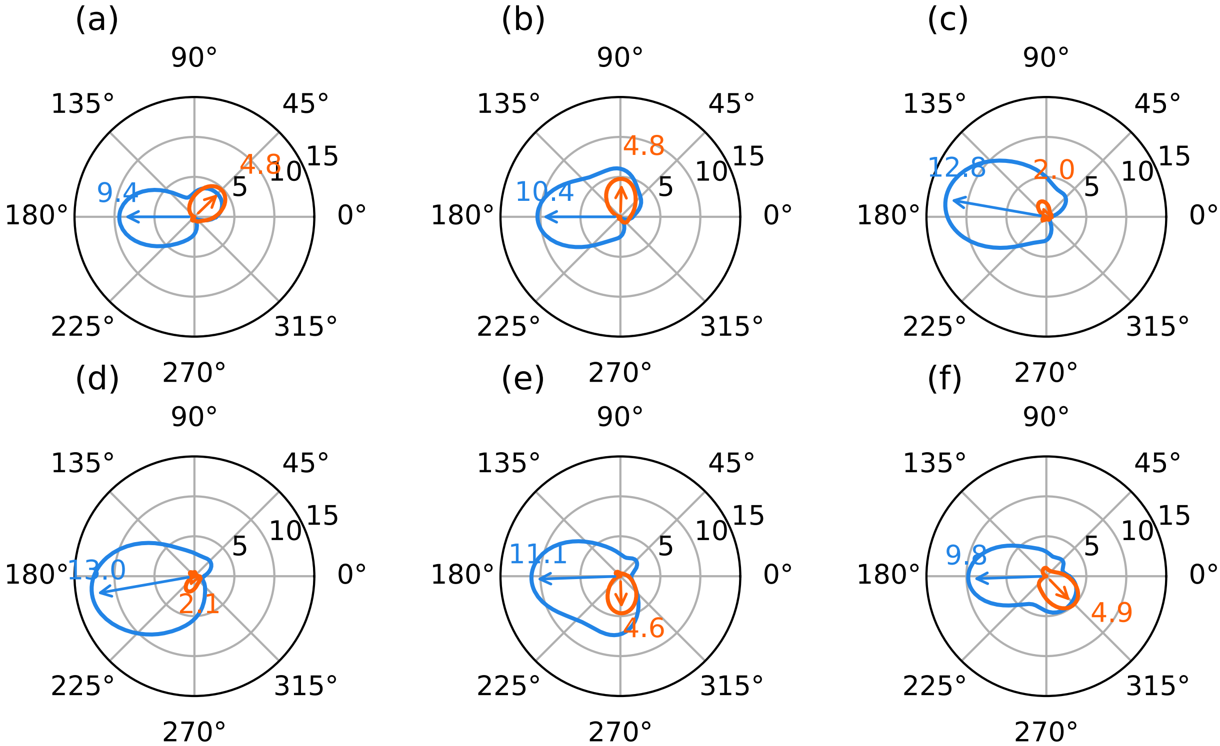

Figure 13. Polar diagrams of amplitudes as the function of propagation directions of the second-round plane wave fit of M_2. The blue lines, arrows and numbers denote the first fit result and the orange denote the second fit result. The amplitudes of the plane waves are the same in panels (a)–(f) but the propagation directions of the second wave range from 90° to 315° with the step of 45°.

with an amplitude of 5 m is generated to do the sensitivity exercises. The size of the fitting window is set to one wavelength of the mode-1 M_2 internal tide. In this study, twice-round plane wave fit is used to distinguish the different M_2 internal tides in different directions. The second fit is applied to the vertical displacement when deleting the displacement induced by the most prominent wave derived from the first fit. Results show that the propagation direction of these two waves could be detected precisely. The amplitude error is relatively large for the angle of the two waves smaller than 45° and zero for larger than 135°. This exercise demonstrated that the plane wave fit with double mode-1 wavelength can distinguish the M_2 internal tides in different propagation directions (Figure 13).

6. Summary and Discussion

Based on multi-year observations of underwater gliders, the spatial distribution of internal tides and their role in mixing in the northern SCS is investigated. Results reveal that the mode-1 diurnal internal tides characterized by ~300 km wavelength in the middle basin are generated at the Luzon Strait (LS) and propagate to the western SCS over 1,000 km. The propagation direction and the magnitude of the energy flux of mode-1 diurnal internal tides are consistent with previous satellite studies (Z. Zhao, 2014). The semidiurnal internal tides have multiple generation regions which are mainly generated at LS in the east and continental shelf and island in the west. The energy of mode-1 diurnal internal tides decays rapidly in the regions within 450 km of the LS while slowly starting after that. This energy decay feature is almost consistent with the numerical model result, which contributes to the local generations of the internal tides (Xu et al., 2016). The glider-based result indicated that the strong energy decay may be also influenced by the remotely generated internal tides. The dissipation rate estimated from integrated energy flux is about 10^{-8} W/kg, consistent with *in-situ* observations in this region (Y. Liu et al., 2017; Lu et al., 2021; Tian et al., 2009). The results indicate the important role of mode-1 diurnal internal tides in inducing far-field mixing in the northern SCS. Note that the estimated dissipation rate is an upper bound value because it is based on a series of assumptions that may overestimate the result. The mission date of the gliders within June to December, which make the result may induce a seasonal bias. Therefore, to further detect the character of the internal tides, a broader range of glider missions need to be launched both in time and regions.

Data Availability Statement

The ETOPO1 bathymetric dataset is available on the National Centers for Environmental Information (NCEI) website (https://ngdc.noaa.gov/mgg/global/global.html). The WOA18 dataset used for modal decomposition is available on the NCEI website (https://www.ncei.noaa.gov/access/world-ocean-atlas-2018/). The barotropic tide model TPXO9 can be downloaded from https://www.tpxo.net/. The underwater glider data used to construct figures in this work are publicly available from Figshare repository (https://figshare.com/articles/dataset/scs_its/23987397).

Acknowledgments

This research is funded by the National Natural Science Foundation of China (42225601, 42076009, 42176006, and 52005365), National Key Research and Development Program of China (2021YFC3101103). ZC is partly supported by the Supporting Funds for Leading Talents (2022GJJLJRC02-014). We are grateful to the three anonymous reviewers for suggestions that let to clarification and improvement of the paper.

References

Alford, M. H. (2003). Redistribution of energy available for ocean mixing by long-range propagation of internal waves. *Nature*, *423*(6936), 159–162. https://doi.org/10.1038/nature01628

Alford, M. H., Peacock, T., MacKinnon, J. A., Nash, J. D., Buijsman, M. C., Centurioni, L. R., et al. (2015). The formation and fate of internal waves in the South China Sea. *Nature*, *521*(7550), 65–69.

Boettger, D., Robertson, R., & Rainville, L. (2015). Characterizing the semidiurnal internal tide off Tasmania using glider data: Tasmanian internal tides in glider data. *Journal of Geophysical Research: Oceans*, *120*(5), 3730–3746. https://doi.org/10.1002/2015JC010711

Egbert, G. D., & Erofeeva, S. Y. (2002). Efficient inverse modeling of Barotropic Ocean tides. *Journal of Atmospheric and Oceanic Technology*, *19*(2), 183–204. https://doi.org/10.1175/1520-0426(2002)019<0183:EIMOBO>2.0.CO;2

Gill, A. E. (1982). *Atmosphere-ocean dynamics* (p. 662). Academic.

Huang, X., Wang, Z., Zhang, Z., Yang, Y., Zhou, C., Yang, Q., et al. (2018). Role of mesoscale eddies in modulating the semidiurnal internal tide: Observation results in the Northern South China Sea. *Journal of Physical Oceanography*, *48*(8), 1749–1770. https://doi.org/10.1175/JPO-D-17-0209.1

Johnston, T. M. S., & Rudnick, D. L. (2015). Trapped diurnal internal tides, propagating semidiurnal internal tides, and mixing estimates in the California Current System from sustained glider observations, 2006–2012. *Deep Sea Research Part II: Topical Studies in Oceanography*, *112*, 61–78. https://doi.org/10.1016/j.dsr2.2014.03.009

Johnston, T. M. S., Rudnick, D. L., Alford, M. H., Pickering, A., & Simmons, H. L. (2013). Internal tidal energy fluxes in the South China Sea from density and velocity measurements by gliders. *Journal of Geophysical Research: Oceans*, *118*(8), 3939–3949. https://doi.org/10.1002/jgrc.20311

Johnston, T. M. S., Rudnick, D. L., & Kelly, S. M. (2015). Standing internal tides in the Tasman Sea observed by gliders. *Journal of Physical Oceanography*, *45*(11), 2715–2737. https://doi.org/10.1175/JPO-D-15-0038.1

Klymak, J. M., Alford, M. H., Pinkel, R., Lien, R.-C., Yang, Y. J., & Tang, T.-Y. (2011). The breaking and scattering of the internal tide on a continental slope. *Journal of Physical Oceanography*, *41*(5), 926–945. https://doi.org/10.1175/2010JPO4500.1

Klymak, J. M., Moum, J. N., Nash, J. D., Kunze, E., Girton, J. B., Carter, G. S., et al. (2006). An estimate of tidal energy lost to turbulence at the Hawaiian ridge. *Journal of Physical Oceanography*, *36*(6), 1148–1164. https://doi.org/10.1175/JPO2885.1

Li, W., & Xie, X. (2023). Reflection and scattering of low-mode internal tides on the continental slope of the South China Sea. *Journal of Physical Oceanography*, *1*(aop), 2687–2699. https://doi.org/10.1175/JPO-D-23-0087.1

Liu, F., Wang, Y., Wu, Z., & Wang, S. (2017). Motion analysis and trials of the deep sea hybrid underwater glider Petrel-II. *China Ocean Engineering*, *31*(1), 55–62. https://doi.org/10.1007/s13344-017-0007-4

Liu, Y., Jing, Z., & Wu, L. (2017). The variation of turbulent diapycnal mixing at 18°N in the South China Sea stirred by wind stress. *Acta Oceanologica Sinica*, *36*(5), 26–30. https://doi.org/10.1007/s13131-017-1067-2

Liu, Z., Xu, J., & Yu, J. (2020). Real-time quality control of data from Sea-Wing underwater glider installed with Glider Payload CTD sensor. *Acta Oceanologica Sinica*, *39*(3), 130–140. https://doi.org/10.1007/s13131-020-1564-6

Lu, Y.-Z., Cen, X.-R., Guo, S.-X., Qu, L., Huang, P.-Q., Shang, X.-D., & Zhou, S.-Q. (2021). Spatial variability of diapycnal mixing in the South China Sea inferred from density overturn analysis. *Journal of Physical Oceanography*, *1*(aop). https://doi.org/10.1175/JPO-D-20-0241.1

Munk, W., & Wunsch, C. (1998). Abyssal recipes II: Energetics of tidal and wind mixing. *Deep Sea Research Part I: Oceanographic Research Papers*, *45*(12), 1977–2010. https://doi.org/10.1016/S0967-0637(98)00070-3

Nash, J. D., Alford, M. H., & Kunze, E. (2005). Estimating internal wave energy fluxes in the ocean. *Journal of Atmospheric and Oceanic Technology*, *22*(10), 1551–1570. https://doi.org/10.1175/JTECH1784.1

Rainville, L., Lee, C. M., Rudnick, D. L., & Yang, K.-C. (2013). Propagation of internal tides generated near Luzon Strait: Observations from autonomous gliders. *Journal of Geophysical Research: Oceans*, *118*(9), 4125–4138. https://doi.org/10.1002/jgrc.20293

Rainville, L., & Pinkel, R. (2006). Propagation of low-mode internal waves through the ocean. *Journal of Physical Oceanography*, *36*(6), 1220–1236. https://doi.org/10.1175/JPO2889.1

Rudnick, D. L. (2016). Ocean research enabled by underwater gliders. *Annual Review of Marine Science*, *8*(1), 519–541. https://doi.org/10.1146/annurev-marine-122414-033913

Rudnick, D. L., Johnston, T. M. S., & Sherman, J. T. (2013). High-frequency internal waves near the Luzon Strait observed by underwater gliders: Rudnick et al.: Internal waves observed by gliders. *Journal of Geophysical Research: Oceans*, *118*(2), 774–784. https://doi.org/10.1002/jgrc.20083

Tian, J., Yang, Q., & Zhao, W. (2009). Enhanced diapycnal mixing in the South China Sea. *Journal of Physical Oceanography*, *39*(12), 3191–3203. https://doi.org/10.1175/2009JPO3899.1

Tozer, B., Sandwell, D. T., Smith, W. H. F., Olson, C., Beale, J. R., & Wessel, P. (2019). Global bathymetry and topography at 15 arc sec: SRTM15+. *Earth and Space Science*, *6*(10), 1847–1864. https://doi.org/10.1029/2019EA000658

Vic, C., Naveira Garabato, A. C., Green, J. A. M., Waterhouse, A. F., Zhao, Z., Melet, A., et al. (2019). Deep-ocean mixing driven by small-scale internal tides. *Nature Communications*, *10*(1), 2099. https://doi.org/10.1038/s41467-019-10149-5

Wang, S., Cao, A., Li, Q., & Chen, X. (2021). Reflection of K1 internal tides at the continental slope in the Northern South China Sea. *Journal of Geophysical Research: Oceans*, *126*(7), e2021JC017260. https://doi.org/10.1029/2021JC017260

Wang, S., Yang, M., Niu, W., Wang, Y., Yang, S., Zhang, L., & Deng, J. (2021). Multidisciplinary design optimization of underwater glider for improving endurance. *Structural and Multidisciplinary Optimization*, *63*(6), 2835–2851. https://doi.org/10.1007/s00158-021-02844-z

Xu, Z., Liu, K., Yin, B., Zhao, Z., Wang, Y., & Li, Q. (2016). Long-range propagation and associated variability of internal tides in the South China Sea. *Journal of Geophysical Research: Oceans*, *121*(11), 8268–8286. https://doi.org/10.1002/2016JC012105

10.1029/2023JC020385

Zhao, R., Zhu, X.-H., Park, J.-H., & Li, Q. (2018). Internal tides in the northwestern South China Sea observed by pressure-recording inverted echo sounders. *Progress in Oceanography*, *168*, 112–122. https://doi.org/10.1016/j.pocean.2018.09.019

Zhao, Z. (2014). Internal tide radiation from the Luzon Strait. *Journal of Geophysical Research: Oceans*, *119*(8), 5434–5448. https://doi.org/10.1002/2014JC010014

Zhao, Z. (2020). Southward internal tides in the northeastern South China Sea. *Journal of Geophysical Research: Oceans*, *125*(11), e2020JC016554. https://doi.org/10.1029/2020JC016554

Zhao, Z., Alford, M. H., Girton, J. B., Rainville, L., & Simmons, H. L. (2016). Global observations of open-ocean mode-1 M_2 internal tides. *Journal of Physical Oceanography*, *46*(6), 1657–1684. https://doi.org/10.1175/JPO-D-15-0105.1

Zhao, Z., Alford, M. H., MacKinnon, J. A., & Pinkel, R. (2010). Long-range propagation of the semidiurnal internal tide from the Hawaiian ridge. *Journal of Physical Oceanography*, *40*(4), 713–736. https://doi.org/10.1175/2009JPO4207.1